Wettability control on deformation: Coupled multiphase fluid and granular systems

Tsimur Davydzenka,[1] Samuel Fagbemi,[1] and Pejman Tahmasebi[1,2,*]
[1]*Department of Petroleum Engineering, University of Wyoming, Laramie, Wyoming 82071, USA*
[2]*Department of Civil Engineering, University of Wyoming, Laramie, Wyoming 82071, USA*

(Received 8 July 2019; revised 2 April 2020; accepted 15 June 2020; published 2 July 2020)

Understanding of multiphase flow in porous media is important for a wide range of applications such as soil science, environmental remediation, energy resources, and CO_2 sequestration. This phenomenon depends on the complex interplay between the fluid and solid forces such as gravitational, capillary, and viscous forces, as well as wettability of the solid phase. Such interactions along with the geometry of the medium give rise to a variety of complex flow regimes. Although much research has been done in the area of wettability, its mechanical effect is not well understood, and it continues to challenge our understanding of the phenomena on macroscopic and microscopic scales. In this paper, therefore, the effect of wettability on the deformation of porous media and fluid-fluid patterns is studied through a series of three-dimensional (3D) simulations. To this end, the discrete element method (DEM) and volume of fluid (VOF) are coupled to accurately model free-surface flow interaction in a cylindrical pack of spheres. The fluid-particle interactions are modeled by exchanging information between DEM and VOF, while the effect of wettability is considered to study how it controls fluid displacement. The results indicate that the drag force and deformation in the pack vary with the change in wettability and capillary number. To demonstrate the effect of both wettability and capillary number, a series of numerical experiments were conducted with two capillary numbers and three wettability conditions. Our results show that the drag force was greatest for near extreme wettability conditions, which resulted in a larger deformation.

DOI: 10.1103/PhysRevE.102.013301

I. INTRODUCTION

Fluid flow in porous media is a multivariable problem that depends on various parameters which may result in two distinct displacements, namely the fluid and solid displacements. Such phenomena are referred to as fluid-fluid and fluid-solid interactions and are controlled by fluid composition [1], relative permeability in the multiphase fluid flow [2–4], the morphology of the medium [5–8], mineralogy [9], fluid regime [10], and wettability [11]. Although the importance of wettability and its effect on fluid-fluid displacement has been an area of intense research [11–18], there is not yet sufficient understanding of its effect on porous media deformation. Wettability is a fundamental property that has a profound effect on the interactions between both the solid and the fluid components in porous media. It also controls the spatial distribution of fluids, which in turn affects the flow and subsequent circulation of fluids during dynamic processes [19,20]. These interactions manifest through drainage (i.e., the residing fluid is more wetting to the solid than the invading fluid) and imbibition (i.e., the opposite of drainage) processes. Properties that may be affected by wettability include resistivity, capillary pressure, relative permeability, and rock strength as well as fluid recovery [21–25], dispersion of tracers, irreducible or residual saturations [26–29], and electrical properties [30].

Numerous studies have been conducted to explore the importance of wettability and in general the physics of multiphase flow through porous media. Recent empirical studies include experiments on Hele-Shaw cells packed with glass beads [25], reporting that an increase in contact angle stabilizes fluid invasion into the granular pack in all capillary numbers. In another study using microfluidics devices patterned with vertical posts, it was observed that increasing the wettability of the invading phase leads to a more efficient displacement of the residing fluid up to a critical contact angle, beyond which the trend is reversed, which contributes to cooperative pore filling and corner flow [12]. Similarly, other core-flooding experiments lead to the conclusion that the variation of contact angle and interfacial curvature increases with the local degree of roughness [31]. The drawback, however, to experimental setups is that they are too time demanding, and in some cases they are difficult to replicate. Thus, it is not easy to compare results from different studies.

The wettability effect has also been implemented in computational modeling. For example, it has been employed in pore network models for different flow regimes and has shown that, in mixed-wet cases, abrupt changes in the saturation profiles occur due to discontinuous capillary pressures [32]. This event results in giving the corresponding saturation paths significantly different shapes, and demonstrate that the traditional capillary- pressure–saturation relationship is not valid under dynamic conditions, as predicted using theoretical methods [33]. Instead, one has to employ the nonequilibrium capillary theory, according to which the fluids' pressure difference is a function of the time rate of saturation change [34]. Advances in computational methods have enabled the use of techniques such as smoothed particle hydrodynamics (SPH) methods [35,36] and lattice Boltzmann methods (LBM) [37–39]. Modeling of surface tension, contact angle,

*ptahmase@uwyo.edu

and viscosity in these methods is achieved through interaction forces acting between different particles or lattice nodes. However, despite the convenience of the implementation, they are still underdeveloped in terms of linking fluid-dynamic processes to interaction forces caused by both the fluid and solid. In a similar fashion, the VOF (volume of fluid) method has been employed to study the relationship between the half corner angle of pores and contact angle controlling the temporal evolution of capillary pressure during the invasion of a pore [40].

When fluids flow in pore space, depending on the velocity, viscosity, and wettability, they can induce deformation in the solid phase. Such deformation, given the solid properties, can be significant. For example, fluid-induced deformation in soft matter can cause noticeable displacements [41]. As such, several methods have recently been developed to couple the effect of fluid flow on deformation. One such method is the coupled LBM and discrete element method (DEM) [42–45], which can be used to model granular systems by capturing the grain-scale movements and interactions. In this method, LBM is used to represent fluid phase over a discrete lattice mesh and DEM is employed to model mechanical behavior. The main advantage of this method is that the pore-scale fluid dynamics can be described more realistically and it also allows capturing and quantifying the fine-scale deformation caused by fluid-particle interactions [46,47]. However, this coupling method is still under development, due to the high demands on computational power, as the fluid particles in LBM are required to be much smaller than the solid elements, which makes its application limited for three-dimensional problems. Alternatively, the computational fluid dynamics (CFD) can be integrated with DEM for mechanical modeling and fluid-particle interactions. Here, the locally averaged Navier-Stokes (NS) equations are used to govern the motion of the fluid flow. In this method, local porosities and additional momenta are transferred from DEM to CFD through which the fluid-particle interactions are quantified. This workflow has been applied to a wide spectrum of large-scale problems with the maximum number of particles being 10^8 [48–60].

A more relevant method that has been implemented to model multiphase flow in porous media is DEM-VOF. This method is a combination of DEM and CFD, which is extended by VOF, which allows including more than one fluid at a time. Previous studies that successfully utilized the DEM-VOF method have shown that this method is capable of computing complex three-phase motion and liquid displacement effects [61–67], which makes this method very appealing for our research. In our study, we adopt unresolved CFD to reduce the computational cost as a large pack of particles is considered. As an alternative to the unresolved method, however, one can extend the DEM-VOF by the immersed boundary (IB) method and use resolved mesh to simulate fluid flow in the presence of solid boundaries [68]. In this study, however, we are interested in capturing large-scale fluid-solid features, therefore we use unresolved methodology.

To better understand the effect of wettability on fluid-fluid and fluid-solid displacements, we focus on fluid distribution patterns and drag force through which such effects are quantified. As such, we incorporate the VOF into DEM and treat the immiscible phases as a single fluid with variable properties. The distribution of the phase is described by a fluid function that carries information about the existing phase, and the interface is identified as the region in which the gradient of the fluid function is nonzero. In the presence of a solid phase, the VOF can naturally account for the contact angle by imposing an appropriate boundary condition on the direction of the fluid-function gradient at the solid interface. In other words, the basic idea of VOF is to solve an additional transport equation of the volume fraction of a particular phase, which serves as an indicator of the wet or dry condition in each fluid cell. Our objective here is to demonstrate the capability of the VOF method to reliably reproduce the *main* features of drainage and imbibition while the mechanical effects are explored. We use LIGGGHTS to model the solid part (DEM), and OPENFOAM to model the two-phase flow (VOF).

The remainder of this paper is organized as follows: In Sec. II we discuss the methodology that we follow for conducting the simulations, mainly the CFD and DEM equations. Section III focuses on presenting the results obtained using our models. Finally, Sect. IV summarizes this paper.

II. METHODOLOGY

In our simulation, as shown in Fig. 1, we have two domains, namely the fluid and particle fields. The cells that are completely covered by particles are assigned a "void fraction" of zero ($\gamma = 0$) and those grid blocks which are partially covered by particles are assigned a void fraction with a value proportional to the covered area. Grid blocks containing fluid are assigned a void fraction of 1 ($\gamma = 1$). The equations for each domain are explained first. To do so, the solid (DEM) and fluid (VOF) parts are explained separately and then the way they are numerically coupled will be discussed afterward.

A. Discrete element method

The discrete element method (DEM) was first proposed by Cundall and Strack [69]. In the last 40 years, there has been considerable development and application of this approach in solving many micromechanical problems [70] such as soil consolidation [71], erosion [72], debris flow entrainment [73], granular flow mobility [74,75], and soil irregular vibration [76,77]. This method can directly model processes at the grain level and capture the relative translation between the particles. A particle-based DEM analysis involves modeling a granular material using elements that usually have simple geometries, such as disks in a two-dimensional (2D) analysis or spheres in 3D.

The key component in DEM is the overlap assumption, meaning that a small amount of overlap (typically <5% of the particle radius) is allowed based on which the corresponding contact force is calculated. The contact model adopted by the DEM method is a crucial element. Several contact models are used in this context, such as (i) the classical fully elastic Hertzian model, in which any surface interactions between solid particles such as those near contact van der Waals interactions or contact adhesive interactions are neglected [78]; (ii) the Johnson-Kendall-Roberts (JKR) model which is an improved Hertzian model in which the contact is considered to be adhesive [79]; (iii) Bradley's van der Waals model

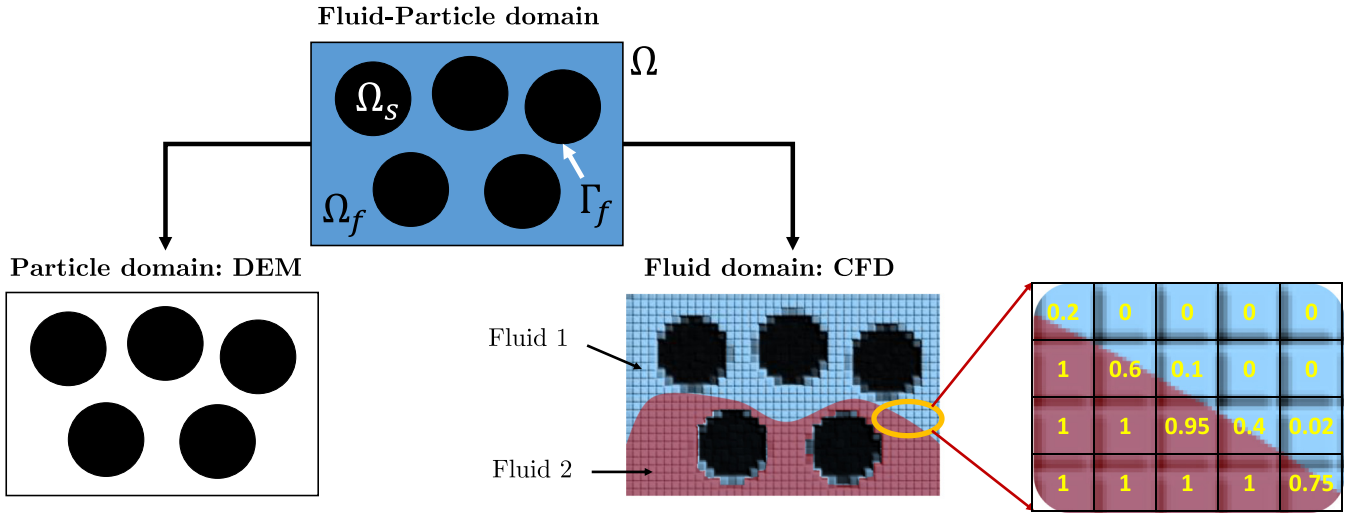

FIG. 1. Decomposition of the whole system into different domains.

in which the elastic material deformations due to the effect of attractive interaction forces are neglected; and (iv) the Derjaguin-Muller-Toporov (DMT) model that is fully elastic and considers adhesion and van der Waals forces [80,81]. The choice of interaction law is determined based on material behavior, experimentation, and experience. In this paper, we employed the Hertzian contact force model as it captures the major features of granular interactions and is more appropriate for the type of studied examples and materials. This method is schematically shown in Fig. 2.

In the case of contact between two spheres, the area of contact is a circle of radius a, as shown in Fig. 2, where E_1 and E_2 are the moduli of elasticity for spheres 1 and 2 of radii R_1 and R_2, and v_1 and v_2 are the Poisson's ratios, respectively.

The maximum contact pressure at the center of the circular contact area is given by

$$P_{\max} = \frac{3F}{2\pi a^2}. \tag{1}$$

In general, when the distance r between two particles of radii R_i and R_j is less than their contact distance $d = R_i + R_j$, the frictional force between them can be calculated using

$$F = (k_n \delta \boldsymbol{n}_{ij} - \varphi_n v\boldsymbol{n}_{ij}) + (k_t \delta \boldsymbol{t}_{ij} - \varphi_t v\boldsymbol{t}_{ij}), \tag{2}$$

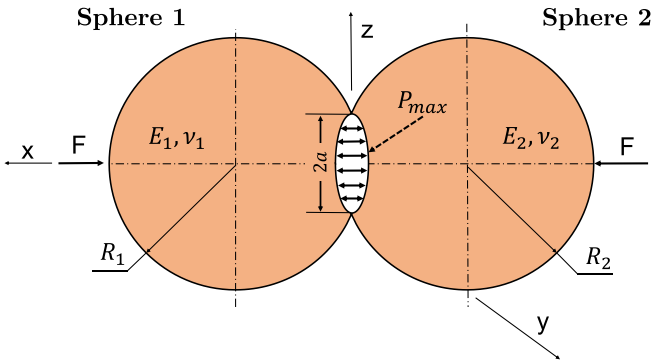

FIG. 2. Contact between two spheres in the Hertzian model implemented in DEM.

where k_n is the elastic constant for normal contact, $\delta \boldsymbol{n}_{ij}$ is normal overlap, φ_n is the viscoelastic damping constant for normal contact, $v\boldsymbol{n}_{ij}$ is normal relative velocity, k_t is the elastic constant for tangential contact, $\delta \boldsymbol{t}_{ij}$ is tangential overlap, φ_t is the viscoelastic damping constant for tangential contact, $v\boldsymbol{t}_{ij}$ is tangential relative velocity, $\boldsymbol{k}_n \delta \boldsymbol{n}_{ij} - \varphi_n v\boldsymbol{n}_{ij}$ denotes normal force, and $\boldsymbol{k}_t \delta \boldsymbol{t}_{ij} - \varphi_t v\boldsymbol{t}_{ij}$ denotes tangential force.

B. Computational fluid dynamics

Computational fluid dynamics (CFD) uses numerical analysis and data structures to analyze and solve problems that involve fluid flows, which has been applied to a wide range of research and engineering problems. In this paper, CFD is coupled with DEM to calculate drag forces. The isothermal motion of an incompressible fluid is described by the divergence-free condition on the fluid velocity:

$$\nabla \cdot \boldsymbol{u} = 0, \tag{3}$$

which expresses the conservation of mass. The momentum equation can be written as

$$\frac{\partial \rho \boldsymbol{u}}{\partial t} + \nabla \cdot (\rho \boldsymbol{u}\boldsymbol{u}) = -\nabla p + \nabla \cdot (2\mu_f \boldsymbol{E}) + \boldsymbol{f}_b, \tag{4}$$

which is derived directly from Newton's second law of motion and describes the conservation of momentum. Here, $\boldsymbol{u}$ is the fluid velocity, ρ is the density, p is the pressure, μ_f is the dynamic viscosity of fluid, $\boldsymbol{E} = (\nabla \boldsymbol{u} + \nabla \boldsymbol{u}^T)/2$ is the rate-of-strain tensor, and $\boldsymbol{f}_b$ accounts for all body forces.

In the presence of two immiscible fluids, characterized by wetting (w) and nonwetting (nw) phases, the fluid domain can be decomposed into several connected bulk-phase regions filled with the individual phases. In any subdomain, the NS equation holds. Therefore, Eqs. (3) and (4) can be written for the specific present phase accordingly. However, one should take a different action on the interfaces between the fluids. In other words, to include two-phase flow in our coupled fluid-particle simulations and take the interfaces of fluid into account, we apply the VOF method, which is a free-surface

modeling technique. The VOF method provides a framework for tracking the interface of a color function moving through a computational grid and a means of applying boundary conditions at the surface. This method allows tracking the shape and position of the interface and quantifying the fraction of each fluid in the interface cells. In other words, VOF aims to provide an equivalent weighted average density and viscosity of individual fluid properties based on their volume fraction in the interface cells. Note that the flux motion should still be solved using the NS equations separately. In the VOF, the volume fraction (or color function) ε is advected by putting the derivative of the fractional function equal to zero:

$$\frac{\partial \gamma}{\partial t} + \nabla \cdot (\gamma \boldsymbol{u}) = 0. \tag{5}$$

This is a Heaviside function that describes the fluid present within a cell. For the primary fluid (phase 1), this value is 1 while the secondary fluid (phase 2) is 0. Fluid cells with values $0 < \varepsilon < 1$ are cells at the interface that accommodate the free fluid surface. Clearly, if a cell is dry, $\varepsilon = 0$, otherwise $\varepsilon = 1$ (the cell is full of liquid). Then, the density and the viscosity are updated and derived based on a linear interpolation with the volume fraction or color function for fluid 1 and fluid 2:

$$\rho(\boldsymbol{x}) = \rho_1 \varepsilon(\boldsymbol{x}) + \rho_2[1 - \varepsilon(\boldsymbol{x})], \tag{6}$$

$$\mu(\boldsymbol{x}) = \mu_1 \varepsilon(\boldsymbol{x}) + \mu_2[1 - \varepsilon(\boldsymbol{x})], \tag{7}$$

where

$$\varepsilon = \frac{1}{V} \int_V \Upsilon(\boldsymbol{x}) d\boldsymbol{x}, \tag{8a}$$

$$\Upsilon = \begin{cases} 1, & \text{the first fluid,} \\ 0, & \text{the second fluid.} \end{cases} \tag{8b}$$

Note that the volume fraction of liquid (ε) is a scalar transported by the local fluid velocity. At the interface between the fluids, Γ, the velocity must be continuous,

$$[\boldsymbol{u}]_\Gamma = \boldsymbol{0}, \tag{9}$$

to obtain the desired nonpenetrating behavior. Here, $[\boldsymbol{u}]_\Gamma$ denotes the jump (i.e., $[x] = x_2 - x_1$) of the quantity in brackets across Γ whereas the stress must satisfy the vector condition

$$[-pI + 2\mu \boldsymbol{E}]_\Gamma \cdot \boldsymbol{n} = \boldsymbol{f}_s, \tag{10}$$

where $\boldsymbol{f}_s$ indicates the capillary force. In this work, the capillary force is solved using the continuum surface force model (CSF) [82], which is defined by

$$\boldsymbol{f}_s = \sigma \kappa \boldsymbol{n}, \tag{11}$$

where σ is the surface tension and $\boldsymbol{n}$ is the normal to the interface, described by

$$\boldsymbol{n} = -\frac{\nabla \varepsilon}{|\nabla \varepsilon|}. \tag{12}$$

The curvature of the fluid-fluid interface κ is defined by

$$\kappa = \nabla \cdot \boldsymbol{n}. \tag{13}$$

To numerically solve the main equation shown in Eq. (5), the advection equation is discretized in a semi-implicit manner. If the equation is solved directly by, e.g., a finite difference method, it can lead to excessive diffusion and smearing at the interface. Thus, an artificial compression term is used to maintain the sharpness of the interface and to prevent interface smearing, which helps to maintain mass conservation and boundedness [83].

One can also include the compressibility term $\boldsymbol{u_r}$ into the VOF, which results in the following form:

$$\frac{\partial(\varepsilon)}{\partial t} + \nabla \cdot (\varepsilon \boldsymbol{u}) + \nabla \cdot [\varepsilon(1 - \varepsilon)\boldsymbol{u}_r] = 0. \tag{14}$$

The artificial compression velocity $\boldsymbol{u}_r$ is given as

$$\boldsymbol{u}_r = \min(C_\tau |\boldsymbol{u}|,\ \max(|\boldsymbol{u}|)) \frac{\nabla \varepsilon}{|\nabla \varepsilon|}, \tag{15}$$

where C_τ is a constant that is used to control the intensity of the fluid's compression. The first two terms on the left side of Eq. (14) have the same advection form as the continuity equation, indicating the fact that in an incompressible fluid the conservation of mass is equivalent to the conservation of volume. The third term can alleviate unnecessary dissipation in the numerical solution. Furthermore, considering the wall adhesion effect, the contact angle between the solid surface and the fluid can be adopted to modify the unit normal $\bar{\boldsymbol{n}}$ of phase interface near the surface:

$$\bar{\boldsymbol{n}} = \bar{\boldsymbol{n}}_w \cos\theta_w + \bar{\boldsymbol{t}}_w \sin\theta_w, \tag{16}$$

where $\bar{\boldsymbol{n}}_w$ is the unit vector normal to the wall, $\bar{\boldsymbol{t}}_w$ is the unit vector tangential to the wall, and θ_w is the contact angle.

C. Coupling CFD and DEM

Studying a coupled behavior of particle and multiphase fluid requires integrating the DEM and CFD sub-systems. In terms of mechanical modeling and DEM, all particles in the computational domain are studied by solving their trajectories. The motion of each particle is governed by

$$m_i \frac{d\boldsymbol{v}_i}{dt} = \sum_{i=1}^{n_i^c} \boldsymbol{F}_{ij}^c + \boldsymbol{F}_i^f + m_i \boldsymbol{g}, \tag{17}$$

$$I_i \frac{d\boldsymbol{\omega}_i}{dt} = \sum_{j=1}^{n_i^c} \boldsymbol{M}_{ij}^c, \tag{18}$$

where $\boldsymbol{v}_i$ is the velocity of particles, $\boldsymbol{F}_{ij}^c$ is contact force on particle i by particle j or walls, $\boldsymbol{F}_i^f$ is the particle-fluid interaction force acting on particle i, $\boldsymbol{g}$ is gravitational acceleration, $\boldsymbol{\omega}_i$ is particle angular velocity, I_i is the moment of inertia, and $\boldsymbol{M}_{ij}$ is the moment acting on particle i by particle j or walls. As mentioned earlier, we applied Hertzian contact force along with Coulomb's friction law in this paper for describing the interaction between particles (i.e., $\boldsymbol{F}_{ij}^c$).

The fluid-particle interaction force $\boldsymbol{F}_i^f$ is the sum of all types of particle-fluid interaction forces acting on individual particles by fluid, including pressure gradient $\boldsymbol{f}_{\nabla p}$, the drag force $\boldsymbol{f}_d$, virtual mass force $\boldsymbol{f}_{\text{vm}}$, viscous force $\boldsymbol{f}_{\nabla \cdot \tau}$ due to the fluid shear stress or deviatoric stress tensor, Basset force $\boldsymbol{f}_B$, and lift forces such as the Saffman force $\boldsymbol{f}_{\text{Saff}}$ and Magnus force $\boldsymbol{f}_{\text{Mag}}$ [84]. The total particle-fluid interaction force on an

individual particle i can be written as

$$\boldsymbol{f}_{pf,i} = \boldsymbol{f}_{\nabla p,i} + \boldsymbol{f}_{d,i} + \boldsymbol{f}_{\mathrm{vm},i} + \boldsymbol{f}_{\nabla\cdot\tau,i} + \boldsymbol{f}_{B,i} + \boldsymbol{f}_{\mathrm{Saff},i} + \boldsymbol{f}_{\mathrm{Mag},i}. \quad (19)$$

In our paper, however, we consider the drag and capillary forces as the most important elements and the other terms of the equation are regarded as negligible.

Due to the contribution of solid particles, we apply the formulation given by Anderson and Jackson [85] to take the presence of multiphase fluid and particles into account. Thus, the NS equations (4) for an incompressible viscous fluid and the advection equation (5) are extended into the following:

$$\frac{\partial(\gamma\rho_f\boldsymbol{u})}{\partial t} + \nabla\cdot(\gamma\rho_f\boldsymbol{u}\boldsymbol{u}) = -\gamma(\nabla p_m + (\boldsymbol{g}\cdot\boldsymbol{x})\nabla\rho_f) + \nabla\cdot(\gamma\boldsymbol{\tau}) + \boldsymbol{f}_s - \boldsymbol{R}_{pf}, \quad (20)$$

where γ is the local porosity. The presence of γ is due to the local average and is defined by

$$\gamma = \left(1 - \frac{1}{V_{\mathrm{cell}}}\sum_{\forall p\in\mathrm{cell}} \boldsymbol{f}_p V_p, \gamma_{\min}\right). \quad (21)$$

To avoid the sharp change of total pressure around the free fluid surface, the term in Eq. (20), namely $\nabla p_m + (\boldsymbol{g}\cdot\boldsymbol{x})\nabla\rho_f$, is rearranged to $-\nabla p + \rho_f\boldsymbol{g}$, where p is the fluid pressure, $p_m = p - \rho_f\boldsymbol{g}\cdot\boldsymbol{x}$ is the modified pressure by rearrangement, and $\boldsymbol{x}$ is the coordinate vector.

As discussed, coupling multiphase fluid and particle requires exchanging a momentum $\boldsymbol{R}_{pf}$ between them, which can be done explicitly or implicitly. The explicit of $\boldsymbol{R}_{pf}$ can be calculated based on the drag model $\boldsymbol{K}_{pf}$ as

$$\boldsymbol{R}_{pf} = \boldsymbol{K}_{pf}(\boldsymbol{u} - \boldsymbol{v}_p), \quad (22)$$

where $\boldsymbol{v}_p$ is the cell-based averaged particle velocity. In this study, the Di Felice drag force model [86] is applied, which has the following form:

$$\boldsymbol{K}_{pf} = \tfrac{1}{8}\kappa_d\rho_f\pi d_p^{-2}|\boldsymbol{u} - \boldsymbol{v}_p|\,\gamma^{1-\xi}. \quad (23)$$

Here, the average diameter of particles in one CFD cell is given by d_p, and the particle-fluid drag coefficient is defined as

$$\kappa_d = \left(0.63 + \frac{4.8}{\sqrt{\mathrm{Re}_p}}\right)^2. \quad (24)$$

The void fraction γ is considered explicitly in the particle Reynolds number Re_p:

$$\mathrm{Re}_p = \frac{\gamma\rho_f d_p|\boldsymbol{u} - \boldsymbol{v}_p|}{\mu_f}. \quad (25)$$

And ξ is a corrective coefficient given by

$$\xi = 3.7 - 0.65\exp\left(-\frac{(1.5 - \log_{10}\mathrm{Re}_p)^2}{2}\right). \quad (26)$$

To solve the equation of drag force produced by fluid, the CFD equations are used on a uniformly discretized collocated finite volume mesh. In this paper, the PISO (pressure-implicit with splitting of operators) algorithm is used for calculating the pressure and velocity in the NS equations. The algorithm consists of one predictor phase and two corrector steps to satisfy mass conservation [87]. Briefly, first, using pressure and velocity fields from previous time steps, the momentum equation is solved, producing a predicted velocity field. Momentum equation (20) can be rewritten as

$$a_P^{\boldsymbol{u}}\boldsymbol{u}_P = \boldsymbol{H}(\boldsymbol{u}) - \gamma\nabla p_m - \gamma(\boldsymbol{g}\cdot\boldsymbol{x})\nabla\rho_f + \boldsymbol{f}_s - \boldsymbol{R}_{pf}, \quad (27)$$

where $a_P^{\boldsymbol{u}}$ and $\boldsymbol{H}(\boldsymbol{u})$ are derived from the discretized algebraic equation. Here, $a_P^{\boldsymbol{u}}$ denotes a matrix coefficient that is related to the centroid point being solved, and $\boldsymbol{H}(\boldsymbol{u}) = \nabla\cdot(\gamma\boldsymbol{\tau}) - \sum_N a_N^{\boldsymbol{u}}\boldsymbol{u}_N$ is composed of a source part $\nabla\cdot(\gamma\boldsymbol{\tau})$ and a transport part $\sum_N a_N^{\boldsymbol{u}}\boldsymbol{u}_N$. The matrix coefficient connects the neighboring centroids multiplied by their velocities. Predicted velocity is defined by

$$\boldsymbol{u}_P = \left[a_P^{\boldsymbol{u}}\right]^{-1}[\boldsymbol{H}(\boldsymbol{u}) - \gamma\nabla p_m - \gamma(\boldsymbol{g}\cdot\boldsymbol{x})\nabla\rho_f + \boldsymbol{f}_s - \boldsymbol{R}_{pf}]. \quad (28)$$

Then, the pressure field is updated during the pressure correction process. When predicted velocity is substituted into the continuity equation (5), the pressure equation reads

$$\nabla\cdot\left\{\gamma^2\left[a_P^{\boldsymbol{u}}\right]^{-1}\nabla p_m\right\} = \nabla\cdot\left\{\left[a_p^{\boldsymbol{u}}\right]^{-1}[\boldsymbol{H}(\boldsymbol{u}) - \gamma V p_m - \gamma(\boldsymbol{g}\cdot\boldsymbol{x})\nabla\rho_f + \boldsymbol{f}_s - \boldsymbol{R}_{pf}]\right\} + \frac{\partial\gamma}{\partial t}. \quad (29)$$

Finally, the velocity field is updated according to the new pressure field obtained from Eq. (29) and, following conservation laws, fluxes are calculated.

One of the assumptions in this study is ignoring the torque exerted from fluid on particles as the pressure gradients produced by fluid around a particle are not considerable compared to the solid angular inertia. Furthermore, since a large number of particles are used, the mechanical variables in the fluid are all presented as an ensemble of average values, which indicates that a few particles can be found in one CFD cell.

Our proposed CFD-DEM for multiphase flow and considering the effect of wettability is shown in Fig. 3. First, a pack of a granular system is generated using the DEM and the particles are allowed to settle based on gravity. Then, the position of each particle is stored, based on which the contacts and overlaps are identified to be used in Eqs. (17) and (18) for computing the new positions and velocities. This step proceeds for a certain number of cycles (n) before the required parameters (e.g., porosity and momentum) are transferred to CFD. Before that, the VOF is used, i.e., Eq. (14), to build and update the free fluid surface. Next, the PISO algorithm, i.e., Eqs. (28) and (29), is utilized to extract the fluid velocity iteratively, which can be used to calculate the fluid force exerted on each particle. The calculated drag force is transferred to DEM to be used in the next time step.

III. RESULTS AND DISCUSSIONS

Due to the importance of adhesive and cohesive forces, one can classify the wettability of a solid surface as weakly, intermediate, or strongly wet. In the cases of strongly and

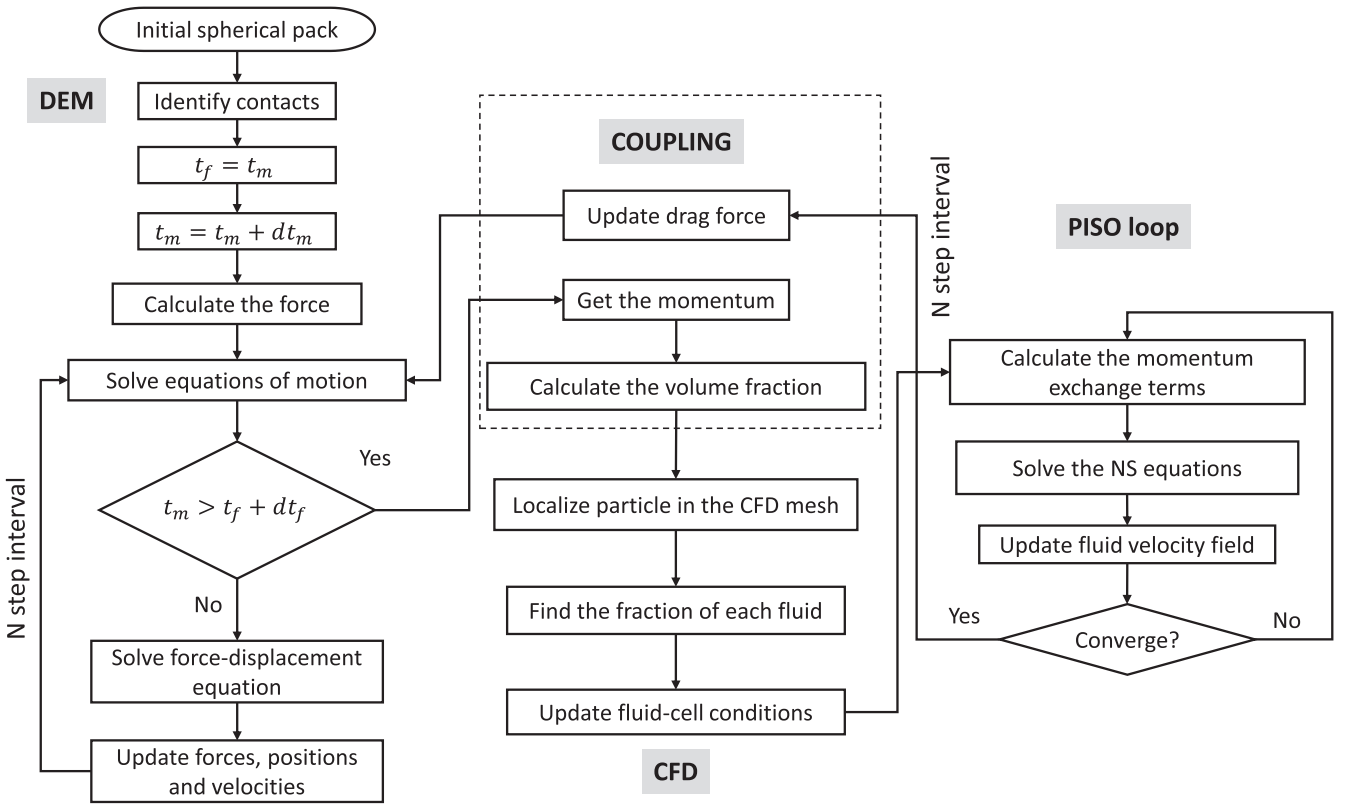

FIG. 3. The diagram of the proposed CFD-DEM method integrated with VOF for micromechanical modeling for a single cycle (i.e., time step).

weakly wet conditions, one of the fluids has a much greater affinity toward a solid surface. If, on the other hand, both fluids exhibit a similar affinity toward the solid surface, the surface is characterized as intermediate wet. Strongly and weakly wet conditions control different pore-scale displacement mechanisms such as snap-off [88,89], pistonlike displacement [90], Haines jump [91], droplet fragmentation [92], cooperative pore filling [93], and corner flow [12].

The contact angle between two fluids measured on a flat surface is a major indicator of wettability in porous media [12]. The relationship between contact angle and surface tension can be mathematically defined according to the Young-Dupre law as $\sigma_{SG} - \sigma_{LS} = \sigma_{LG}\cos(\theta)$, where σ_{SG} is the surface tension between the residing fluid and solid surface, σ_{SL} is the interfacial tension between the invading and residing fluid, and σ_{LG} is the surface tension between the invading fluid and solid surface; see Fig. 4.

A. Dimensionless numbers

The VOF method described above is implemented to perform numerical simulations of drainage and imbibition. The dynamics of the displacement largely depend on the properties of the two fluids and the injection rate. For a given porous media, the displacement processes depend mostly on the interplay between viscous and capillary forces. The parameters that are generally used to characterize flow behavior are contact angle, capillary number

$$\mathrm{Ca} = \frac{\mu_{in}\boldsymbol{u}_{in}}{\sigma}, \tag{30}$$

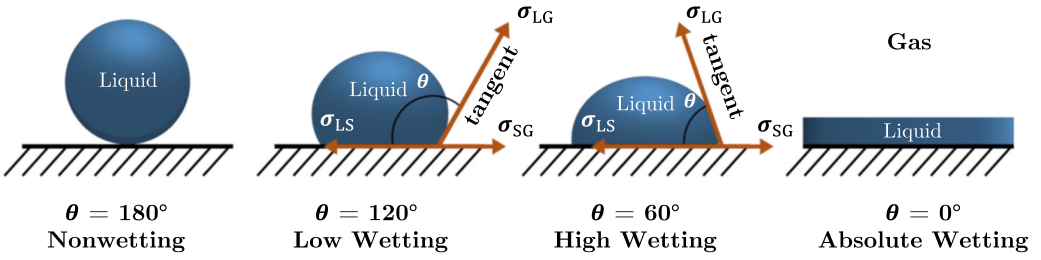

FIG. 4. Different wettability conditions.

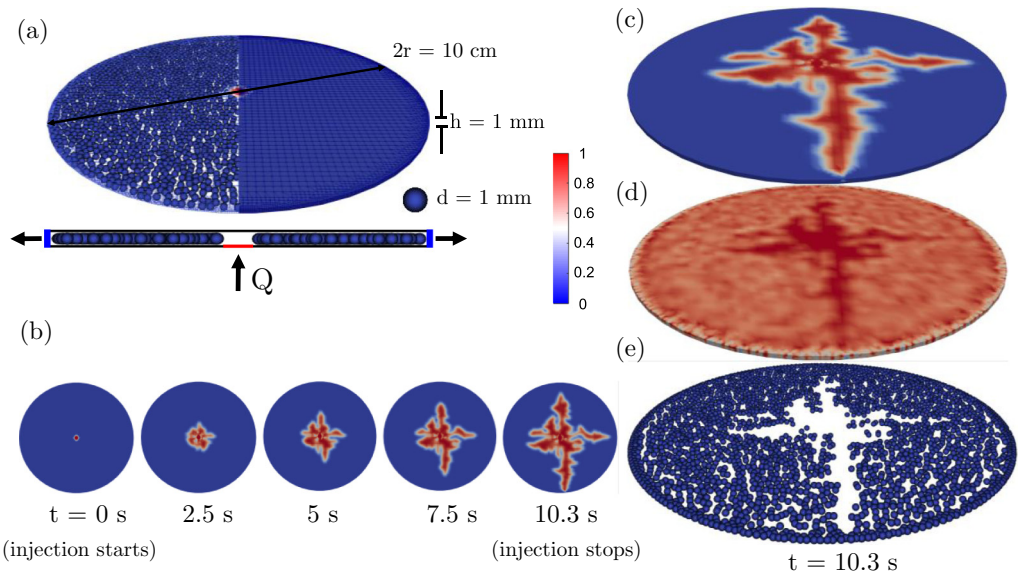

FIG. 5. Demonstration of the computational domain (a) with solid particles and unresolved CFD mesh represented as a wireframe on the left side (for particle visibility) and as the surface with edges on the right. An example of $\theta = 150^{\circ}$, Ca = 4.5 is presented in (b) with snapshots of volume fraction for the injected fluid (water), corresponding to $t = 0,\ 2.5,\ 5,\ 7.5,\ 10.3$ s. Volume fraction, void fraction, and particles' positions snapshots for the last time step of the simulation are presented in (c), (d), and (e). A color bar in the center of the figure is applicable for parts (a), with initial volume fraction in the center of the domain, (b), (c), and (d).

and the ratio of the dynamic viscosity of the invading phase μ_{in} to that of the residing phase μ_{res},

$$M = \frac{\mu_{\text{inj}}}{\mu_{\text{res}}}, \tag{31}$$

where μ_{in} is the dynamic viscosity of the invading fluid, $\boldsymbol{u}_{in}$ is velocity, and σ is surface tension. Both the viscosity ratio and capillary number control the stability of the displacement front. Capillary number Ca quantifies the relative difference between capillary and viscous forces.

B. Computational domain

We use a semi-2D cylindrical pack with 4660 spherical particles having the following properties: density $= 10^5$ kg/m^3, diameter $= 0.5$ mm, Young's modulus $= 5\times10^6$ Pa, Poisson's ratio $= 0.45$, restriction coefficient $= 0.3$, and friction coefficient $= 0.5$. The solid model is shown in Fig. 5(a). Pack size was chosen to be 1 mm high and 10 cm in diameter. The simulation domain was initially saturated with silicon oil (receding phase) and water (invading phase) in the center of the domain prior to the actual injection. The numerical experiments are conducted until the injected phase reaches the outer boundaries of the domain. The fluid is injected from the center of the pack with the rates $Q = 0.3$ and 3 ml/min. A plane at the bottom, placed in the center of the domain, is used as the inlet, while the fluid patches in a radial direction are designated as the outlet. For the part of our models where deformation of the pack is not considered, particles are fixed at their initial locations and remain motionless throughout the injection. To be able to quantify deformation in the pack, for the part of our models where deformation is studied, the particles can move based on the exerted drag force. To find a compromise between a very small and very significant movement of the particles in the pack, we vary the density of the particles and find 10^5 kg/m^3 to be a proper choice in our case. In Table I we have listed the fluid properties that are used in the CFD component of our simulations.

Before presenting the results, we conducted a sensitivity analysis on the effect of the number of cells for the CFD simulations. Grid independence analysis has shown that the optimal number of cells for our simulation is approximately 26 000, with an average size of 1.1 mm^3. As can be seen from Fig. 6, injection pressure becomes unstable and does not follow the trend observed in the experimental study [12] as the mesh becomes finer than a certain number of cells per domain, which is due to using a resolved mesh with an unresolved fluid solver.

C. Results

In this section, we present the results for two-phase fluid interaction with the monodisperse particles domain under different wettability conditions. First, we validate the results

TABLE I. Properties of the fluid used in the simulations.

Property	Value(s)
Contact angle, θ (degrees)	7, 60, 150
Surface tension, σ (kg s^{-2})	0.013
Viscosity of the invading phase, ν_w (m^2 s^{-1})	1×10^{-6}
Viscosity of the residing phase, ν_{air} (m^2 s^{-1})	3.54×10^{-4}
Density of the invading phase, ρ_w (kg m^{-2})	1000
Density of the residing phase, ρ_{air} (kg m^{-2})	960
Capillary number, Ca	4.5, 0.45

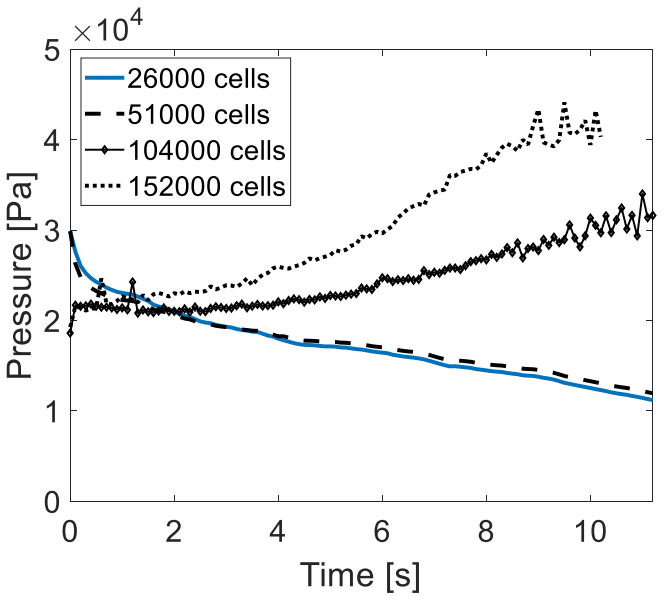

FIG. 6. Grid independence analysis.

of our method against a well-reviewed experimental study. Further, we quantify the results obtained for cases with and without deformation, and we compare and analyze them. The validation of our results is conducted based on a previous experimental study performed by Zhao *et al.* [12] by creating a pack of monodisperse particles as a way to reproduce solid walls and replicate all of the remaining conditions. In our study, due to using an unresolved mesh for VOF, the wettability effect of particles is presented as an average property and their fine-scale features are not captured. In other words, since the upper and lower walls of the pack are much larger than the implemented mesh, they completely manifest the wettability effect, whereas a set of particles falls in a single mesh cell. We also use adjusted injection rates due to pore volume differences.

To make the comparison easier, we include the validation results for injection pressure evolution as well, based on which a direct comparison can be made. The results are shown in Fig. 7. Figures 7(a) and 7(d) are provided by the experimental study referenced earlier, and Figs. 7(b) and 7(e) correspond to our computational results. One can observe that the general trend of injection pressure evolution is in agreement with the experiments. Moreover, the results for the higher capillary number are found to be very close to the experimental data. Results for the smaller capillary number, on the other hand, are in agreement with the experiments to a lesser degree. Such discrepancy can be observed in terms of the time that it takes the fluid to reach the outer boundaries of the domain. This observation, however, can be explained by the fact that, as the

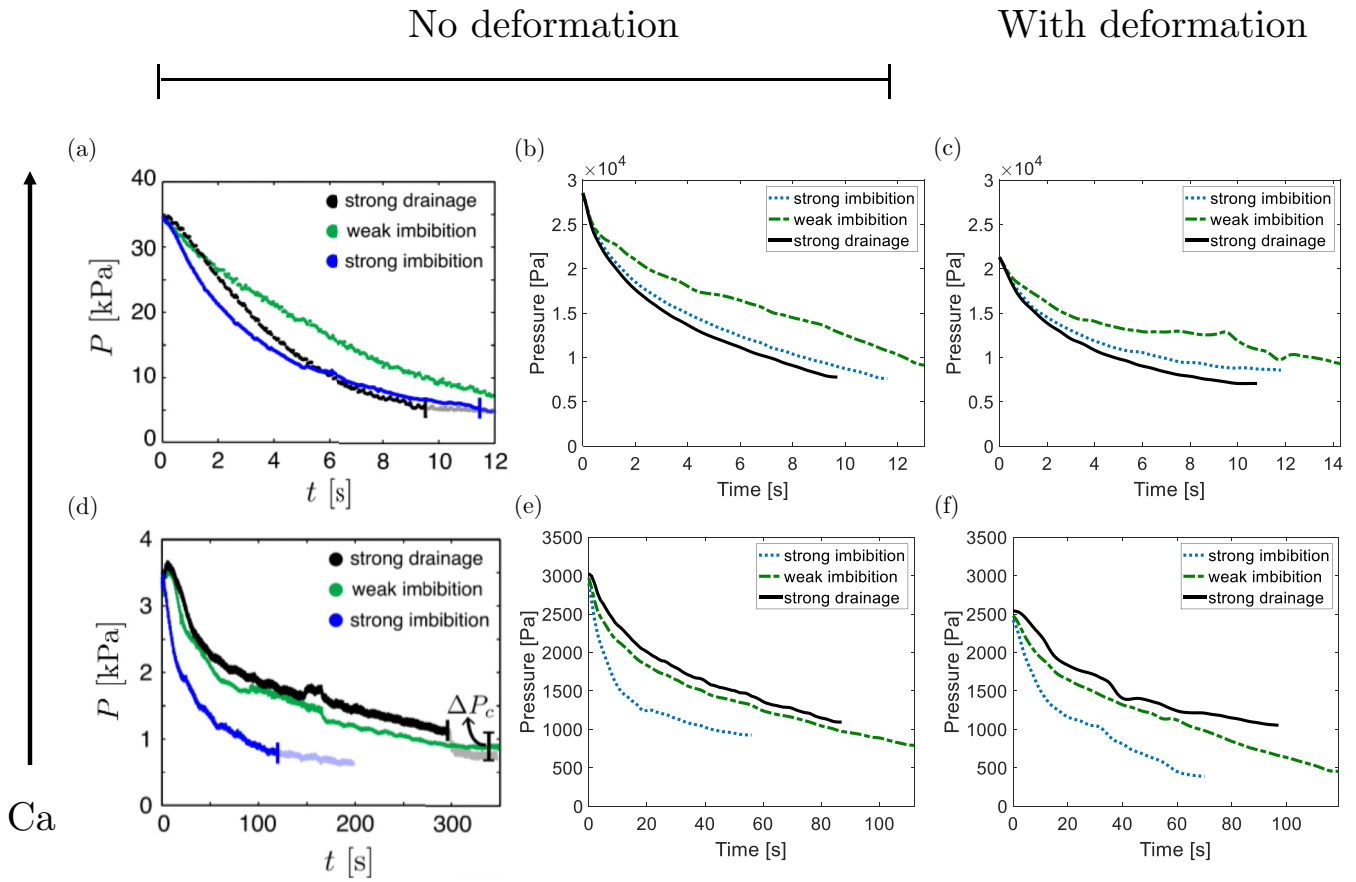

FIG. 7. Validation of injection pressure evolution. Plots (a) and (d) are for the experimental results and (b), (c), (e), (f) show computational results. (b) and (e) represent results for equivalent experimental conditions, and (c) and (f) are the results for the same computational conditions as (b) and (e), but with allowed particle movement.

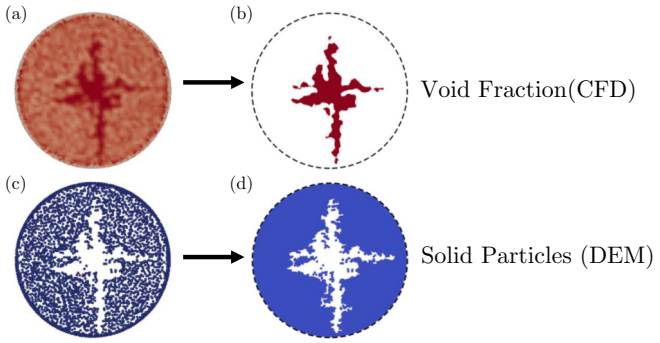

FIG. 8. Demonstration of the decomposition of a pack's void fraction (a) and solid particles' position (b) snapshots into regions (c) and (b) that are subsequently used for red (void fraction) and white (particles positions) pixel count.

injection rates drop, capillary forces begin to have a greater impact on the dynamic processes in a porous system, which means it becomes more challenging for our method to capture such features with greater precision. Finally, the results of the topic of this paper, namely the effect of wettability in a coupled environment, are presented in Figs. 7(c) and 7(f), wherein the particles are allowed to displace. As can be seen, injection pressure in the very first time steps of the simulation is 10–25% smaller than in the nondeformation (fixed) models. This considerable pressure drop is related to the fact that, as particles are allowed to move in the domain, the injected fluid is no longer forced to propagate in small channels created by the presence of particles, rather it opens up new pores by pressing the particles. Therefore, as injection proceeds, the previously small channels are replaced with newly formed larger channels created by the movement of the particles. However, as the injected fluid propagates through the domain, the pressure difference between cases with and without deformation becomes less noticeable, as the pack becomes more and more packed while the particles are not allowed to leave the domain. Furthermore, we observe that for some of the cases the injection pressure is higher than in the corresponding nondeforming cases, which is again in accordance with the fact that, by the end of the simulation, the pack becomes very packed at its outer boundaries and pressure has to build up before the fluid can propagate.

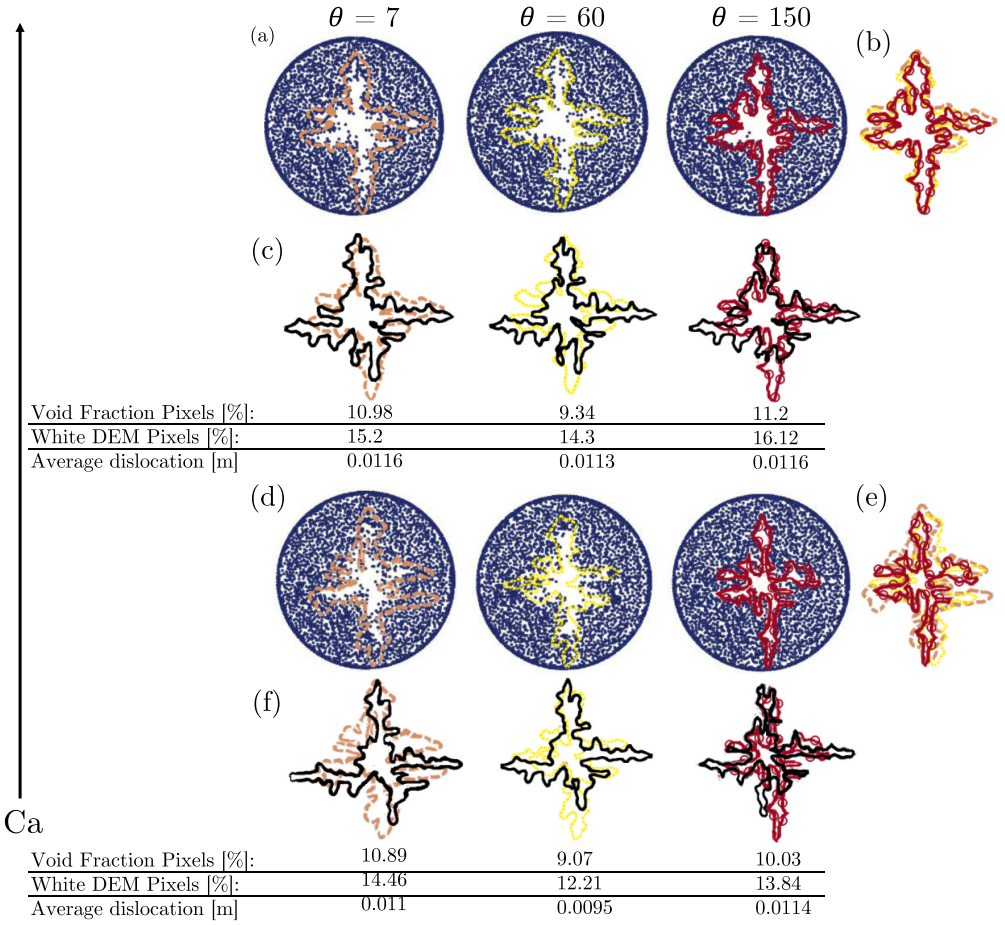

	$\theta = 7$	$\theta = 60$	$\theta = 150$
Void Fraction Pixels [%]:	10.98	9.34	11.2
White DEM Pixels [%]:	15.2	14.3	16.12
Average dislocation [m]	0.0116	0.0113	0.0116

	$\theta = 7$	$\theta = 60$	$\theta = 150$
Void Fraction Pixels [%]:	10.89	9.07	10.03
White DEM Pixels [%]:	14.46	12.21	13.84
Average dislocation [m]	0.011	0.0095	0.0114

FIG. 9. Comparison between the deformations. (a) and (d) show the final positions of particles for Ca = 4.5, 0.45, respectively, and different wettability conditions. The dashed brown, dotted yellow, and circled red lines represent the contours of volume fraction [i.e., Figs. 5(b) and 5(c)] for its respective cases ($\theta = 7^\circ,\ 60^\circ,\ 150^\circ$). (c) and (f) are contours of volume fraction propagation in the packs, with dashed brown, dotted yellow, and circled red lines corresponding to cases with deformation, and *solid black* lines corresponding to cases without deformation. (b) and (e) show contours of volume fraction for cases with deformation for Ca = 4.5, 0.45 with dashed brown, dotted yellow, and circled red lines corresponding to $\theta = 7^\circ,\ 60^\circ,\ 150^\circ$ cases respectively.

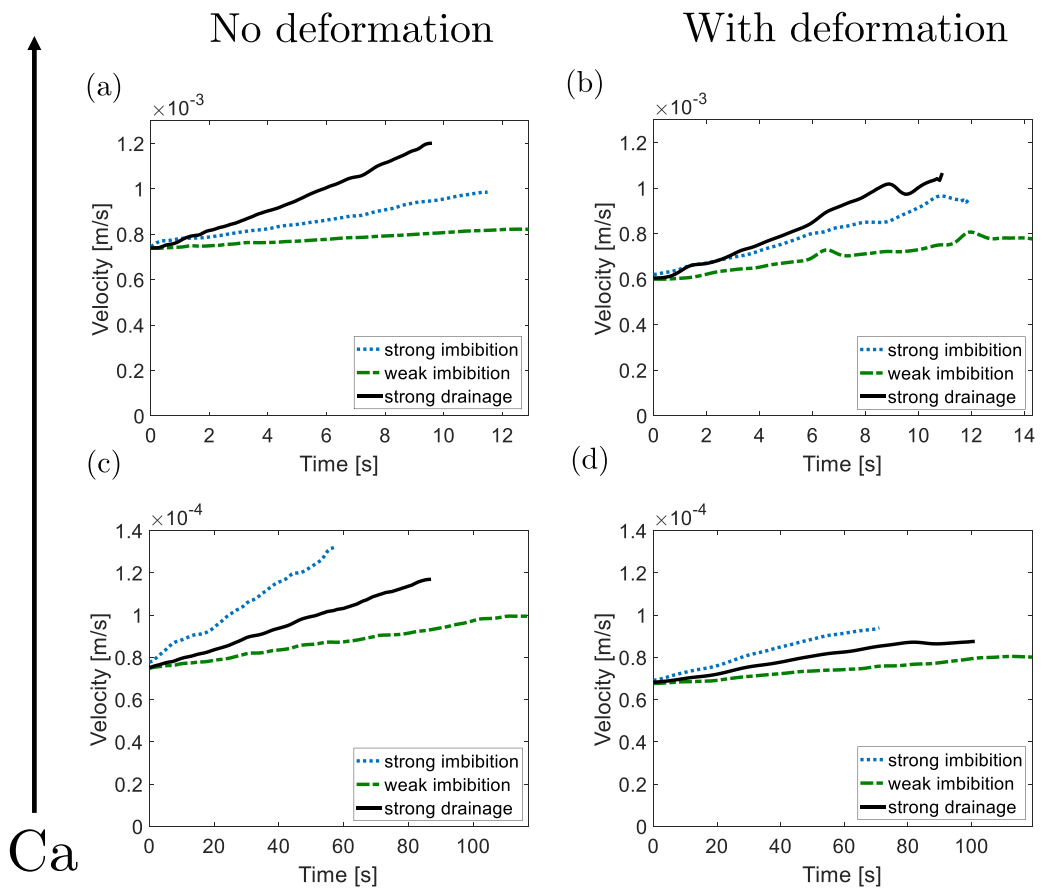

FIG. 10. Average velocity evolution for cases without deformation [(a) and (c)] and with deformation [(b) and (d)]. Plots (a) and (b) are for Ca = 4.5 and plots (c) and (d) are for Ca = 0.45.

To observe and quantify the effect of wettability and capillary number on deformation, and to be able to quantify the size of possible fractures created by the injected fluid, we use a pixel count method to count the red pixels in void fraction data and white pixels in particles positions. Figure 8 illustrates the procedure for the pixel count. Furthermore, we calculated the average travel distance of particles in the pack. These observations are provided in Fig. 9. Figures 9(a) and 9(d), respectively, represent the final particles' positions for Ca = 4.5, 0.45 and $\theta = 7^\circ,\ 60^\circ,\ 150^\circ$ (left to right). Each case is provided with the deformation values in the table underneath it. It can be noted that for the two capillary numbers the maximum deformation is observed in those packs with wettability conditions close to the extreme values. For the higher capillary number the maximum deformation is achieved when $\theta = 150^\circ$ (strong drainage), and for the smaller Ca the greatest deformation observed was for $\theta = 7^\circ$ (strong imbibition).

The trend of the maximum deformation for cases of extreme wettability conditions can be explained by the fact that, in both of these extreme wettability scenarios, velocity manifests a larger magnitude, with the highest value for strong drainage in the Ca = 4.5 case, and the highest value for strong imbibition in the Ca = 0.45 case. In Figs. 9(b) and 9(e), we include superimposed contours of volume fraction for the cases with deformation under different wettability conditions to better visualize the effect of the wettability. As can be seen, at the higher capillary number, the difference between water propagation patterns is less noticeable than for the smaller capillary number cases. This particular observation is related to the importance of capillary forces and wettability at smaller injection rates, as velocity becomes less important in the propagation.

To further quantify the effects of deformation, we include average velocity and drag force evolution plots in Figs. 10 and 11. It can be seen from the results that, for every wettability and injection condition, the average velocity decreases when the movement of the particles is allowed, and consequently it takes more time for the fluid to reach the outer boundaries. Furthermore, to validate our results with the experimental study discussed earlier, the highest average velocity for all the cases considered is observed when wettability conditions are near extremes. Accordingly, the highest values of drag forces were recorded for $\theta = 7^\circ$ and 150°.

IV. CONCLUSIONS

Flow in porous media is influenced by several parameters. Wettability is one of such properties that controls the transport behavior. In this paper, the effect of wettability was studied in a series of systematic examples using a coupling method to explore how deformation in porous media is affected by wettability when a complex system of a two-phase fluid exists. To this end, the simulation was divided into two parts to take into account the effects of fluid-particle, particle-particle,

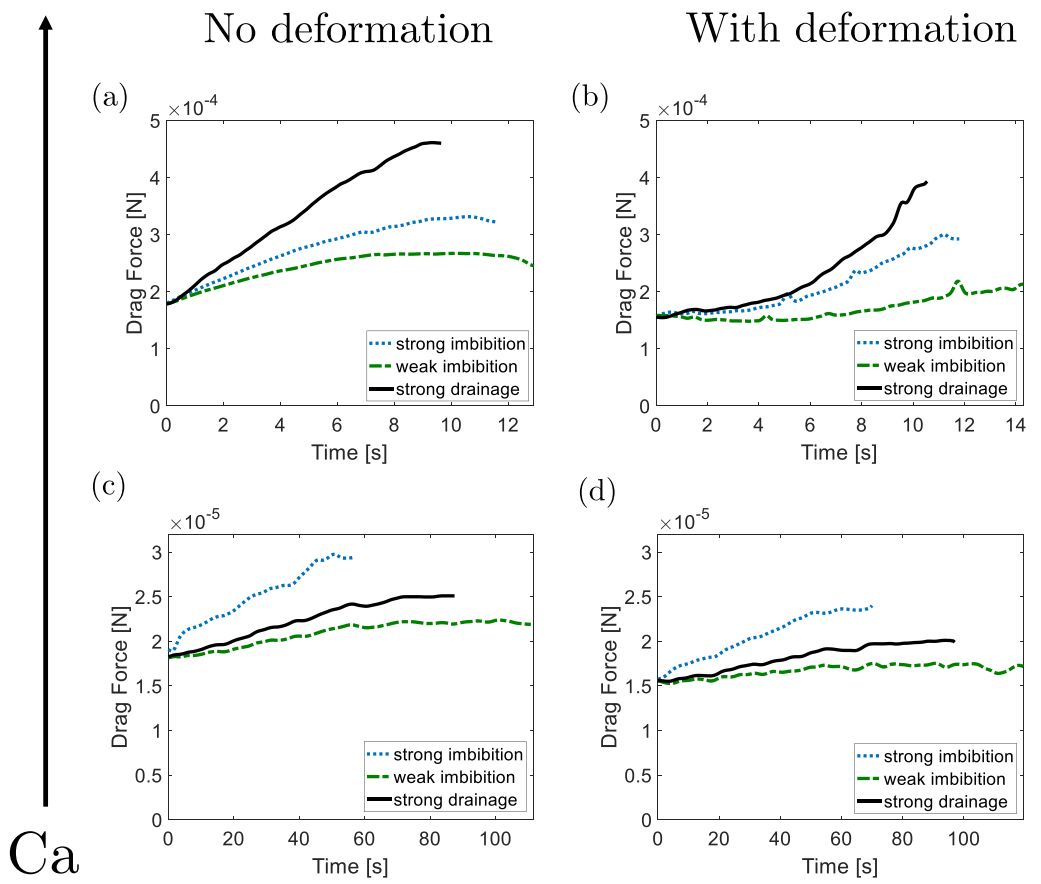

FIG. 11. Drag force evolution for cases without deformation [(a) and (c)] and with deformation [(b) and (d)]. Plots (a) and (b) are for Ca = 4.5 and plots (c) and (d) are for Ca = 0.45.

and fluid-fluid interactions. As such, DEM and VOF were applied to simulate the behavior of the solid and fluid phases, respectively. The result of this coupling helps to enrich our understanding of the overall pore-scale fluid dynamics controlling the deformation mechanisms under various injection and wettability conditions.

Our VOF method relies only on conservation principles, classic surface tension, and contact-angle models, which can accurately track the fluid-fluid interactions. The advantage of the VOF method over other flow through porous media methods (e.g., SPH) is that it provides information at a finer scale by representing the fluid in a more realistic way, which ensures model accuracy. Furthermore, this method enables us to extend the simulation area to a larger region through which studying complex systems become more reliable with real phenomena. Our proposed method enables us eventually to reconstruct the fine-scale features and fluid behavior by upscaling.

As a result of this study, the following observations were made:

(i) The maximum drag force was achieved when the medium was strongly wet and strongly nonwet for the invading fluid.

(ii) Propagation of the invading fluid largely depends on the wettability of the medium, and its effect becomes more noticeable as capillary numbers decrease. For all wettability conditions, the observed trend of fluid displacement pattern indicates that as the wettability reaches its extreme values the pack gets invaded more easily, which is confirmed and validated by the results of injection pressure evolution.

ACKNOWLEDGMENTS

We would like to express thanks for the financial support from the University of Wyoming for this research. The critical review from the anonymous reviewers that led to improving the initial submission is greatly acknowledged. This study was partially supported by NSF (Grant No. CMMI-2000966), NIH (Grant No. P20GM103432), and NASA (Grant No. 80NSSC19M0061).

[1] S. Abaci, J. S. Edwards, and B. N. Whittaker, Mine Water Environ. **11**, 11 (1992).

[2] R. Hu, Y. Chen, H. Liu, and C. Zhou, Sci. China Technol. Sci. **58**, 1971 (2015).

[3] R. Lenormand, C. Zarcone, and A. Sarr, *Mechanisms of the Displacement of One Fluid by Another in a Network of Capillary Ducts* (Cambridge University Press, Cambridge, 1983).

[4] R. Lenormand, E. Touboul, and C. Zarcone, J. Fluid Mech. **189**, 165 (1988).

[5] J. Hommel, E. Coltman, and H. Class, Transp. Porous Media **124**, 589 (2018).

[6] X. Zhang and P. Tahmasebi, Int. J. Greenhouse Gas Control **76**, 266 (2018).

[7] X. Zhang and P. Tahmasebi, Transp. Porous Media **129**, 321 (2019).

[8] P. Tahmasebi and S. Kamrava, Int. J. Greenhouse Gas Control. **83**, 245 (2019).

[9] I. Aksu, E. Bazilevskaya, and Z. T. Karpyn, GeoResJ **7**, 1 (2015).

[10] W. A. Moseley and V. K. Dhir, J. Hydrol. **178**, 33 (1996).

[11] J. Zhao, Q. Kang, J. Yao, H. Viswanathan, R. Pawar, L. Zhang, and H. Sun, Water Resour. Res. **54**, 1295 (2018).

[12] B. Zhao, C. W. MacMinn, and R. Juanes, Proc. Natl. Acad. Sci. USA **113**, 10251 (2016).

[13] C.-X. Zhao, Adv. Drug Delivery Rev. **65**, 1420 (2013).

[14] R. Holtzman, Sci. Rep. **6**, 36221 (2016).

[15] Y. Qi, X. Luo, Y. Wang, N. Liu, B. Zhou, J. Yan, and L. Zhang, Int. J. Multiphase Flow **93**, 205 (2017).

[16] S. A. Bradford, L. M. Abriola, and F. J. Leij, J. Contam. Hydrol. **28**, 171 (1997).

[17] M.-H. Huit and M. J. Blunt (unpublished).

[18] G. Camps-Roach, D. M. O'Carroll, T. A. Newson, T. Sakaki, and T. H. Illangasekare, Water Resour. Res. **46**, W08544 (2010).

[19] C. McPhee, J. Reed, and I. Zubizarreta, *Core Analysis: A Best Practice Guide* (Elsevier, Amsterdam, 2015).

[20] S. Fagbemi and P. Tahmasebi, J. Fluid Mech. **897**, A20 (2020).

[21] P. Chen and K. Mohanty, SPE J. **18**, 124 (2013).

[22] N. Morrow and J. Buckley, J. Pet. Technol. **63**, 106 (2011).

[23] D. C. Standnes and T. Austad, J. Pet. Sci. Eng. **28**, 123 (2000).

[24] D. C. Standnes and T. Austad, Colloids Surf. A **216**, 243 (2003).

[25] M. Trojer, M. L. Szulczewski, and R. Juanes, Phys. Rev. Appl. **3**, 054008 (2015).

[26] P. P. Jadhunandan and N. R. Morrow, SPE Reservoir Eng. **10**, 40 (1995).

[27] J. S. Buckley, Y. Liu, and S. Monsterleet, SPE J. **3**, 54 (1998).

[28] E. J. Manrique, V. E. Muci, and M. E. Gurfinkel, SPE Reservoir Eval. Eng. **10**, 667 (2007).

[29] E. J. Spiteri, R. Juanes, M. J. Blunt, and F. M. Orr, SPE J. **13**, 277 (2008).

[30] A. L. Ogunberu and M. Ayub, Pet. Sci. Technol. **23**, 169 (2005).

[31] A. AlRatrout, M. J. Blunt, and B. Bijeljic, Proc. Natl. Acad. Sci. USA **115**, 8901 (2018).

[32] P. Tahmasebi and S. Kamrava, Phys. Rev. E **98**, 052901 (2018).

[33] R. Holm, M. I. J. van Dijke, and S. Geiger, Transp. Porous Media **81**, 423 (2010).

[34] H. K. Joekar-Niasar, V. Hassanizaden, and S. M. Dahle, J. Fluid Mech. **655**, 38 (2010).

[35] A. M. Tartakovsky and P. Meakin, Adv. Water Resour. **29**, 1464 (2006).

[36] U. C. Bandara, A. M. Tartakovsky, and B. J. Palmer, Int. J. Greenhouse Gas Control **5**, 1566 (2011).

[37] C. Pan, M. Hilpert, and C. T. Miller, Water Resour. Res. **40**, W01501 (2004).

[38] B. Ahrenholz, A. Peters, A. Kaestner, M. Krafczyk, and W. Durner, Adv. Water Resour. **31**, 1151 (2008).

[39] M. L. Porter, M. G. Schaap, and D. Wildenschild, Adv. Water Resour. **32**, 1632 (2009).

[40] H. S. Rabbani, V. Joekar-Niasar, and N. Shokri, J. Colloid Interface Sci. **473**, 34 (2016).

[41] J. Bueno, Y. Bazilevs, R. Juanes, and H. Gomez, Extreme Mech. Lett. **13**, 10 (2017).

[42] A. Hassanpour, H. Tan, A. Bayly, P. Gopalkrishnan, B. Ng, and M. Ghadiri, Powder Technol. **206**, 189 (2011).

[43] G. T. Houlsby, Comput. Geotech. **36**, 953 (2009).

[44] C. H. Rycroft, A. V. Orpe, and A. Kudrolli, Phys. Rev. E **80**, 031305 (2009).

[45] L.-S. Lu and S.-S. Hsiau, Particuology **6**, 445 (2008).

[46] Y. Han and P. A. Cundall, Int. J. Numer. Anal. Methods Geomech. **37**, 1391 (2013).

[47] E. Oñate, D. Owen, E. Ramm, P. Wriggers, A. Leonardi, F. K. Wittel, M. Mendoza, and H. J. Herrmann, in *Proceedings of the 3rd International Conference on Particle-Based Methods: Fundamentals and Applications (PARTICLES 2013), Stuttgart, 18–20 September, 2013* (CIMNE, Barcelona, 2013).

[48] K. W. Chu, B. Wang, A. B. Yu, and A. Vince, Powder Technol. **193**, 235 (2009).

[49] C. Wu, Y. Cheng, Y. Ding, and Y. Jin, Chem. Eng. Sci. **65**, 542 (2010).

[50] J. Zhao and T. Shan, Powder Technol. **239**, 248 (2013).

[51] Z. B. Tong, B. Zheng, R. Y. Yang, A. B. Yu, and H. K. Chan, Powder Technol. **240**, 19 (2013).

[52] H. Li, Y. Li, F. Gao, Z. Zhao, and L. Xu, Comput. Electron. Agric. **88**, 111 (2012).

[53] C. T. Jayasundara, R. Y. Yang, B. Y. Guo, A. B. Yu, I. Govender, A. Mainza, A. van der Westhuizen, and J. Rubenstein, Miner. Eng. **24**, 181 (2011).

[54] K. W. Chu, B. Wang, D. L. Xu, Y. X. Chen, and A. B. Yu, Chem. Eng. Sci. **66**, 834 (2011).

[55] X. Ku, T. Li, and T. Løvås, Chem. Eng. Sci. **122**, 270 (2015).

[56] M. H. Zhang, K. W. Chu, F. Wei, and A. B. Yu, Powder Technol. **184**, 151 (2008).

[57] D. Jajcevic, E. Siegmann, C. Radeke, and J. G. Khinast, Chem. Eng. Sci. **98**, 298 (2013).

[58] Y. Zhao, Y. Ding, C. Wu, and Y. Cheng, Powder Technol. **199**, 2 (2010).

[59] K. Washino, H. S. Tan, M. J. Hounslow, and A. D. Salman, Chem. Eng. Sci. **93**, 197 (2013).

[60] X. Chen, W. Zhong, X. Zhou, B. Jin, and B. Sun, Powder Technol. **228**, 309 (2012).

[61] X. Sun, M. Sakai, and Y. Yamada, J. Comput. Phys. **248**, 147 (2013).

[62] G. Pozzetti and B. Peters, in *Proceedings of the International Conference of Numerical Analysis and Applied Mathematics (ICNAAM 2016), 19–25 September 2016, Rhodes, Greece*, edited by T. Simos and C. Tsitouras, AIP Conf. Proc. No. 1863 (AIP, New York, 2017), p. 180002.

[63] G. Pozzetti and B. Peters, Int. J. Multiphase Flow **99**, 186 (2018).

[64] L. Li and B. Li, Particuology **39**, 109 (2018).

[65] L. Jing, C. Y. Kwok, Y. F. Leung, and Y. D. Sobral, Int. J. Numer. Anal. Methods Geomech. **40**, 62 (2016).

[66] L. Wu, M. Gong, and J. Wang, Ind. Eng. Chem. Res. **57**, 1714 (2018).

[67] X. Sun and M. Sakai, Chem. Eng. Sci. **134**, 531 (2015).
[68] A. Hager, C. Kloss, S. Pirker, and C. Goniva, in *Proceedings of the 9th International Conference on Computational Fluid Dynamics in the Minerals and Process Industries, 10–12 December 2012, Melbourne, Australia*, edited by C. B. Solnordal, P. Liovic, G. W. Delaney, and P. J. Witt (CSIRO, Canberra, 2012).
[69] P. A. Cundall and O. D. L. Strack, Géotechnique **29**, 47 (1979).
[70] W. Chen and T. Qiu, Int. J. Geomech. **12**, 127 (2012).
[71] Y. Cui, D. Chan, and A. Nouri, Int. J. Geomech. **17**, 04017033 (2017).
[72] Y. Tang, D. H. Chan, and D. Z. Zhu, Int. J. Numer. Anal. Methods Geomech. **41**, 1477 (2017).
[73] F. C. Payne, J. A. Quinnan, and S. T. Potter, *Remediation Hydraulics* (CRC Press, Boca Raton, FL, 2008).
[74] W.-T. Ding and W.-J. Xu, Powder Technol. **335**, 301 (2018).
[75] W.-J. Xu, L.-M. Hu, and W. Gao, Int. J. Rock Mech. Min. Sci. **86**, 166 (2016).
[76] Z. Zhang, X. Zhang, H. Qiu, and M. Daddow, Constr. Build. Mater. **125**, 564 (2016).
[77] Z. Zhang, X. Zhang, Y. Tang, and Y. Cui, J. Zhejiang Univ. A **19**, 346 (2018).
[78] H. Hertz, J. Für Die Reine Und Angew. Math. (J. Pure Appl. Math.) (1881).
[79] K. L. Johnson, K. Kendall, and A. D. Roberts, Proc. R. Soc. A, Math. Phys. Eng. Sci. **324**, 301 (1971).
[80] B. Derjaguin, V. Muller, and Y. Toporov, J. Colloid Interface Sci. **53**, 314 (1975).
[81] V. M. Muller, B. V. Derjaguin, and Y. P. Toporov, Colloids Surf. **7**, 251 (1983).
[82] J. U. Brackbill, D. B. Kothe, and C. Zemach, J. Comput. Phys. **100**, 335 (1992).
[83] H. G. Weller, Technical Report (Imperial College, University of London, 2008).
[84] C. T. Crowe, *Multiphase Flows with Droplets and Particles* (CRC Press, Boca Raton, FL, 2012).
[85] T. B. Anderson and R. Jackson, Ind. Eng. Chem. Fundam. **6**, 527 (1967).
[86] Z. Y. Zhou, S. B. Kuang, K. W. Chu, and A. B. Yu, J. Fluid Mech. **661**, 482 (2010).
[87] R. I. Issa, J. Comput. Phys. **62**, 40 (1986).
[88] P. Hoyer, V. Alvarado, and M. S. Carvalho, Phys. Fluids **28**, 012104 (2016).
[89] S. S. Datta, J.-B. Dupin, and D. A. Weitz, Phys. Fluids **26**, 062004 (2014).
[90] V. Joekar-Niasar and S. M. Hassanizadeh, Crit. Rev. Environ. Sci. Technol. **42**, 1895 (2012).
[91] S. Berg, H. Ott, S. A. Klapp, A. Schwing, R. Neiteler, N. Brussee, A. Makurat, L. Leu, F. Enzmann, J.-O. Schwarz, M. Kersten, S. Irvine, and M. Stampanoni, Proc. Natl. Acad. Sci. USA **110**, 3755 (2013).
[92] T. Pak, I. B. Butler, S. Geiger, M. I. J. van Dijke, K. S. Sorbie, M. I. J. van Dijke, and K. S. Sorbie, Proc. Natl. Acad. Sci. USA **112**, 1947 (2015).
[93] R. Holtzman and E. Segre, Phys. Rev. Lett. **115**, 164501 (2015).